

## XRISM Observations of Abell 1795: Evidence for Low Turbulence and Resonant Scattering

ARNAB SARKAR,<sup>1,2</sup> ERIC D. MILLER,<sup>2</sup> BRIAN MCNAMARA,<sup>3</sup> HELEN RUSSELL,<sup>4</sup> KOTARO FUKUSHIMA,<sup>5</sup> MARK BAUTZ,<sup>2</sup>  
YUTAKA FUJITA,<sup>6</sup> CATHERINE E. GRANT,<sup>2</sup> FRANÇOIS MERNIER,<sup>7,8,9,10</sup> MICHAEL A. McDONALD,<sup>2</sup> NAOMI OTA,<sup>11</sup>  
AYŞEGÜL TÜMER,<sup>12,8,9</sup> AND DANIEL WIK<sup>13</sup>

<sup>1</sup>*Department of Physics, University of Arkansas, 825 W Dickson st., Fayetteville, AR 72701, USA*

<sup>2</sup>*Kavli Institute for Astrophysics and Space Research, Massachusetts Institute of Technology, 70 Vassar St, Cambridge, MA 02139*

<sup>3</sup>*Department of Physics & Astronomy, Waterloo Centre for Astrophysics, University of Waterloo, Ontario N2L 3G1, Canada*

<sup>4</sup>*School of Physics & Astronomy, University of Nottingham, University Park, Nottingham NG7 2RD, UK*

<sup>5</sup>*Institute of Space and Astronautical Science (ISAS), Japan Aerospace Exploration Agency (JAXA), Kanagawa 252-5210, Japan*

<sup>6</sup>*Department of Physics, Tokyo Metropolitan University, Tokyo 192-0397, Japan*

<sup>7</sup>*Department of Astronomy, University of Maryland, College Park, MD 20742, USA*

<sup>8</sup>*NASA / Goddard Space Flight Center, Greenbelt, MD 20771, USA*

<sup>9</sup>*Center for Research and Exploration in Space Science and Technology, NASA / GSFC (CREST II), Greenbelt, MD 20771, USA*

<sup>10</sup>*Univ Toulouse, CNES, CNRS, IRAP, Toulouse, France*

<sup>11</sup>*Department of Physics, Nara Women's University, Nara 630-8506, Japan*

<sup>12</sup>*Center for Space Sciences and Technology, University of Maryland, Baltimore County (UMBC), Baltimore, MD, 21250 USA*

<sup>13</sup>*Department of Physics & Astronomy, University of Utah, 270 South 1400 East, Salt Lake City, UT, 84112, USA*

### ABSTRACT

We present high-resolution X-ray spectroscopic observations of the cool-core galaxy cluster Abell 1795 obtained with XRISM/Resolve. The cluster was observed with two deep pointings: a 225 ks central exposure and a 113 ks northern exposure, extending to a projected radius of 320 kpc from the cluster center. Single-temperature fits reveal a clear radial gradient in the line-of-sight velocity dispersion, decreasing from  $114 \pm 11$  km/s in the core to  $68 \pm 39$  km/s at 320 kpc. The bulk velocities in the central regions are very low ( $22 \pm 12$  and  $7 \pm 21$  km/s), indicating no significant relative motion between the brightest cluster galaxy (BCG) and the intracluster medium (ICM). Given that the central region includes the southward-extending cool gas tail, this result disfavors the “cooling-wake” scenario and instead supports an AGN-uplift origin. We find that the nonthermal pressure fraction decreases with radius, from  $P_{\text{NT}}/P_{\text{T}} \approx 2\%$  in the core to  $\sim 0.6\%$  at 330 kpc, suggesting that the northern ICM of A1795 is largely quiescent. Two-temperature and split energy-band (2–4 keV and 6–7 keV) fits identify two gas phases within the central  $< 1.5'$  region, providing strong evidence for multiphase gas in the cluster core. We detect a  $\sim 14\%$  resonant suppression of the optically thick Fe XXV  $w$  line in the center. Additionally, we observe a significant excess in the Fe XXV  $y$  line-flux relative to models. Accounting for uncertainties in the atomic data reduces this discrepancy, suggesting that atomic data uncertainties may contribute to the observed residual flux.

*Keywords:* Galaxy clusters (573) — Intracluster medium (ICM) (343) — X-ray astrophysics (739)

### 1. INTRODUCTION

Galaxy clusters assemble hierarchically through mergers and ongoing accretion from the cosmic web. The resulting gas dynamics play a key role in the cluster energy budget, as a substantial fraction of the injected kinetic energy is transferred to the intra-cluster medium (ICM), driving bulk motions and turbulence (e.g., F. Vazza et al. 2009, 2018; A. Simionescu et al. 2019; A. Sarkar et al. 2022, 2023, 2025a). The first direct measurement of line-of-sight ICM velocities in a relaxed clus-

ter core provided by Hitomi observations of Perseus indicates that, despite the rich spatial structure revealed by Chandra (J. S. Sanders & A. C. Fabian 2007; J. S. Sanders et al. 2016), the ICM is quiescent, with velocity dispersion less than 200 km/s within the central 100 kpc and non-thermal pressure support of only  $\sim 4\%$ . (e.g., Hitomi Collaboration et al. 2016a, 2018a). These results suggest that the velocity broadening is driven by small-scale motions, with a turbulent driving scale less than 100 kpc, consistent with the size of Active Galactic Nu-

clei (AGN)-driven bubbles; that non-thermal pressure accounts for a small fraction of the total pressure in the core; and that sloshing can explain a modest bulk velocity gradient across the cluster core.

The launch of the XRISM satellite in 2023 has opened up a new opportunity to probe kinematics in other clusters using an instrument with similar spectral capabilities to the Hitomi SXS (M. Tashiro et al. 2025; R. L. Kelley et al. 2025). In the past year, the Resolve microcalorimeter onboard XRISM has revealed line-of-sight (LOS) velocity dispersion measurements in several cool-core clusters such as Abell 209 (XRISM Collaboration et al. 2025a,b; A. Sarkar et al. 2025b), Centaurus (XRISM Collaboration et al. 2025c), Hydra A (T. Rose et al. 2025), and the Ophiuchus cluster (Y. Fujita et al. 2025). Their velocity dispersion estimates lie between 120–190 km/s. Even for merging galaxy clusters like Coma (XRISM Collaboration et al. 2025d) and Abell 3667 (Y. Omiya et al. 2026), the velocity dispersion is  $\sim 200$  km/s. These findings, while groundbreaking, highlight our lack of understanding about how the effects of AGN feedback, merger-induced sloshing, and other dynamical activity conspire to shape the spatial and kinematic structure of clusters on all scales. We can address this by dramatically expanding the sample of clusters with accurate direct velocity measurements.

Abell 1795 (A1795 hereafter) is a nearby ( $z = 0.062$ ), relatively hot (spatially-averaged  $kT \approx 5.3$  keV; A. Vikhlinin et al. 2006; S. L. Snowden et al. 2008; M. W. Bautz et al. 2009) cool-core cluster. It is one of a handful of clusters with very deep Chandra observations, exceeding 3.4 Msec, due to its use as a regular calibration source. Several studies have utilized this dataset and extensive multiwavelength coverage to paint a picture of a complex core of activity within the inner 100 kpc ( $1.4'$ ) as illustrated in Figure 1 (see also: S. A. Walker et al. 2014; S. Ehlert et al. 2015; G. Kokotanekov et al. 2018a). Multiple AGN-blown cavities are seen along with radio emission whose spectral signatures suggest several episodes of AGN activity. A 50-kpc-long tail of cool X-ray-emitting plasma extends south of the Brightest Cluster Galaxy (BCG), spatially coincident with striking H $\alpha$  filaments and ending in a hook-shaped feature (M. McDonald & S. Veilleux 2009; S. Ehlert et al. 2015). This tail is thought to arise from a cooling wake left either by the fast-moving BCG as it plows through the inner ICM, or related to an observed sloshing cold front in the inner part of the cluster (M. Markevitch et al. 2001). On even smaller scales, ALMA reveals two massive molecular gas filaments that trace the edges of the inner radio bubbles within 10 kpc of the AGN (H. R. Russell et al. 2017a). These filaments exhibit a smooth velocity gra-

dient spanning 450 km/s, and they are thought to result from low-entropy X-ray gas that has been entrained by the expanding bubbles, become thermally unstable, and cooled. A recent study of stellar and nebular emission line kinematics suggests a similar range of line-of-sight velocities for these populations (P. D. Tamhane et al. 2023a).

In this paper we present XRISM/Resolve observations of the central and northern region of A1795. We focus on the ICM kinematics and resonant scattering of the cool core and regions immediately outside of the cool core. Throughout the paper, we adopt a  $\Lambda$ CDM cosmology with  $H_0 = 70$  km s $^{-1}$  Mpc $^{-1}$ ,  $\Omega_m = 0.3$ , and  $\Omega_\Lambda = 0.7$ . At the redshift of A1795 ( $z = 0.062$ ),  $1'$  corresponds to 69 kpc. All reported redshifts and velocities have been corrected to the solar system barycenter. We also adopt K. Lodders & H. Palme (2009) proto-solar abundance table. Unless otherwise noted, all uncertainties are reported at the  $1\sigma$  (68%) confidence level.

## 2. DATA REDUCTION

XRISM observed Abell 1795 through two pointings: one central pointing on 2025 January 22–27 for 226 ks (OBSID 201087010) and one northern pointing on 2025 January 20–22 for 113 ks (OBSID 201088010). Table 1 shows a complete observation log. The data were reprocessed with the `xpipeline` tool in HEASoft v6.36 (N. H. E. A. S. A. R. Center 2014), adopting the most recent calibration database (CalDB v20250915) for Resolve. Following the recommendations in the XRISM ABC Guide v1.0<sup>§§§</sup>, we screened the event data for cross-talk events using the specified `RISE_TIME`, `DERIV_MAX`, and `STATUS` column filtering criteria.

For each observation, spectra were extracted from the full array and sub-arrays, excluding Pixel 27, which has historically exhibited anomalous gain shifts not aligned with the timing of the filter wheel  $^{55}\text{Fe}$  gain fiducial exposures. Pixel 11 also occasionally displays similar abrupt scale variations, therefore it is also excluded from our analysis (A. Sarkar et al. 2025b). Our analysis includes only high-resolution primary (Hp; `ITYPE=0`) events, which comprise more than 99% of the 2–10 keV event population in each observation. For background, a non-X-ray background (NXB) spectrum was generated for each observation using the `rslnxbgen` tool. Instrumental responses were generated for each observation using `rslmkrmf` with the most up-to-date calibration database (CalDB v20250915). The redistribution matrix file (RMF) was scaled by

<sup>§§§</sup> [https://heasarc.gsfc.nasa.gov/docs/xrism/analysis/abc\\_guide/xrism\\_abc.html](https://heasarc.gsfc.nasa.gov/docs/xrism/analysis/abc_guide/xrism_abc.html)

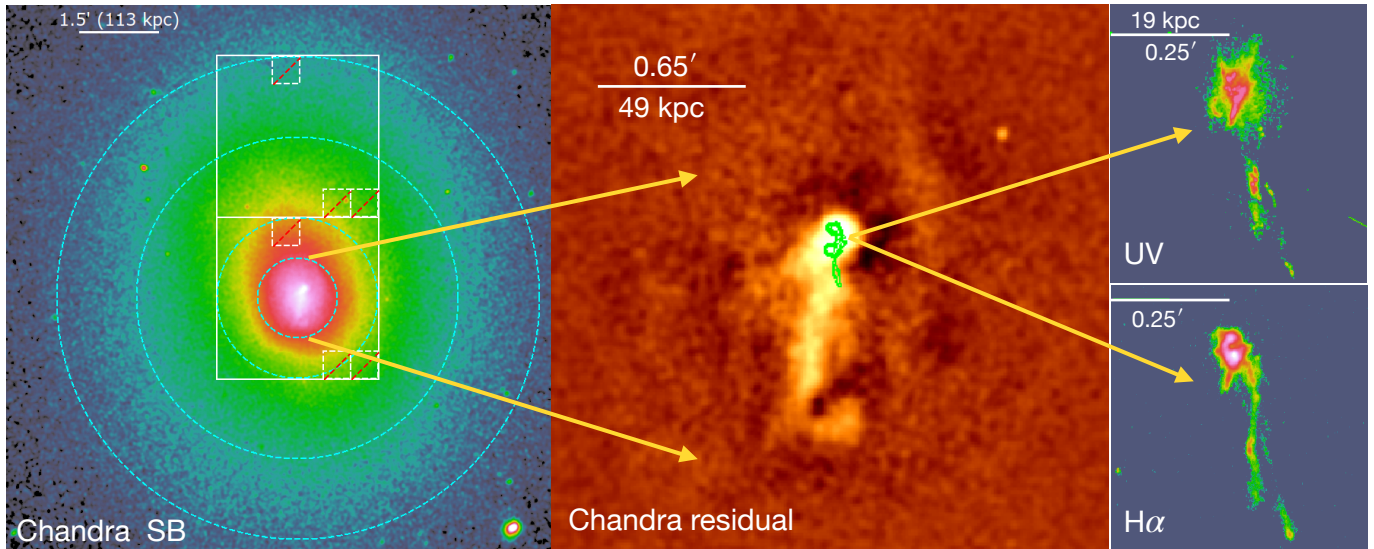


**Figure 1.** Left: Exposure corrected and background subtracted Chandra image of A1795 in the 0.5–10 keV energy band. Resolve FoVs are marked with white boxes. Dashed small white boxes show the excluded pixels 11, 12 (calibration pixel), and 27. Cyan dashed annuli shows the regions used for ARFs generation. Right: Zoomed in residual image of A1795 after subtracting a beta model image. Several substructures including the ‘hook’ are clearly seen. Green contours represent the ALMA CO(2–1) contours from H. R. Russell et al. (2017b).

**Table 1.** XRISM Observation logs

Pointing	Observation ID	RA (deg)	Decl. (deg)	Observation Date	Exposure (ks)
Central	201087010	207.21837	26.59235	2025-01-22–2025-01-27	225.8
North 1	201088010	207.21804	26.64328	2025-01-20–2025-01-22	113.3

the fraction of high-resolution primary (Hp) events in the 2–10 keV band—excluding low-resolution secondary (Ls) events—to properly account for the exclusion of medium- and low-resolution events and ensure accurate flux normalization.

### 3. SPECTRAL FITTING

Spectral fitting was performed using `XSpec 12.15.1` (K. A. Arnaud 1996). We extracted spectra from the pixels in the central and northern pointings that lie within each annulus with radii of  $0'–0.75'$ ,  $0.75'–1.5'$ ,  $1.5'–3'$ , and  $3'–4.5'$ , as shown in Figure 1. Given the modest point-spread function of the Resolve X-ray mirror assembly (Half Power Diameter  $\sim 1.3'$ , M. Tashiro et al. 2025), spatial spectral mixing (SSM) was taken into account following A. Sarkar et al. (2025b). We used four annuli regions, as shown in Figure 1, to model the ICM emission corresponding to each extracted Resolve spectrum. We generated ancillary response files (ARFs) with `xaarfgen` in image mode, adopting the 2–10 keV Chandra image as the input sky brightness distribution. The `xaarfgen` task internally calls `xrtraytrace`

to ray-trace photons through the X-ray Mirror Assembly and `xaxmaarfgen` to compute the net effective area for the selected Resolve detector regions, including detector efficiencies. To account for the broad Resolve point-spread function and the resulting spatial mixing, we computed ARFs for each pairwise combination of input and extraction regions shown in Figure 1. These region-dependent ARFs were then used in `XSPEC` to fold each model component through the appropriate response. For more details on `xrtraytrace` tool, we refer readers to XRISM abc guide<sup>111</sup>.

The spectrum from each region was fitted with an absorbed single-temperature (1T) `TBABS × BAPEC` model. We note that `BAPEC` model accounts for the thermal broadening. For each region, the temperature, abundance, redshift, velocity dispersion ( $\sigma_v$ ), and normalization were allowed to vary freely. The hydrogen column density,  $N_H$ , was fixed to the Galactic value of  $1.2 \times 10^{20} \text{ cm}^{-2}$  (HI4PI Collaboration et al. 2016).

<sup>111</sup> [heasarc.gsfc.nasa.gov/docs/xrism/analysis/quickstart](https://heasarc.gsfc.nasa.gov/docs/xrism/analysis/quickstart)

In addition, the spectrum from each region was fitted with an absorbed two-temperature (2T) TBABS  $\times$  (BAPEC+BAPEC) model. The non-X-ray background (NXB) was modeled by fitting the NXB spectrum with a power law and multiple Gaussian components representing instrumental lines, simultaneously with the source emission. Similarly, the unresolved Cosmic X-ray Background (CXB) was modeled using a power law with a photon index of  $\Gamma = 1.41$  and a scaled-normalization adopted from Suzaku measurements (M. W. Bautz et al. 2009). We ignored the effect of Galactic foreground components since our spectral fitting is limited to  $> 2$  keV. The best-fit parameters and their confidence intervals for each region were obtained by minimizing the C-statistic (W. Cash 1979). Table 2 lists the best-fit parameters obtained from the 1T and 2T fits, together with their  $1\sigma$  uncertainties. Figure 2 shows the best-fit 1T models along with the Resolve spectra for each region. Figure 3 shows the zoomed in version with the linear y-axes.

## 4. RESULTS AND DISCUSSION

### 4.1. ICM velocity structure

The velocity dispersion measurements from Resolve spectra are primarily constrained by the Fe-K line complexes in the 6–8 keV energy band. Figure 4 presents the best-fit velocity dispersion,  $\sigma_v$ , as a function of radius from the cluster center. A1795 exhibits remarkably low velocity dispersion ( $\sim 50\text{--}90$  km s $^{-1}$ ) just outside the central Resolve pointing ( $\gtrsim 100$  kpc), comparable to values reported for A2029 (XRISM Collaboration et al. 2025b; A. Sarkar et al. 2025b). Within the central 100 kpc, the measured  $\sigma_v$  values ( $\sim 115$  km s $^{-1}$ ) are consistent with but on the low end of those observed in other clusters, including Ophiuchus (Y. Fujita et al. 2025), Perseus (Hitomi Collaboration et al. 2016b), Centaurus (XRISM Collaboration et al. 2025c), and A2029 (XRISM Collaboration et al. 2025a,b; A. Sarkar et al. 2025b). XRISM Collaboration et al. (2025e) compared measured velocity dispersions of cool-core cluster centers with predictions from cosmological simulations, finding systematically lower velocities in the observed clusters. Our measurement of a low velocity dispersion in A1795’s core further strengthens the possible tension between the simulations and measured gas kinematics.

We adopt a redshift of  $0.063001 \pm 0.000223$  for the BCG of A1795. This redshift corresponds to an observed barycentric systemic velocity of  $cz = 18887 \pm 67$  km/s. This value is derived from stellar population synthesis modeling of XSHOOTER spectra extracted from the central region of the BCG (P. D. Tamhane et al. 2023b). All bulk velocities reported in this paper are

measured relative to this systemic velocity using the expression

$$v_{\text{bulk}} = \frac{c(z - z_{\text{BCG}})}{1 + z_{\text{BCG}}}, \quad (1)$$

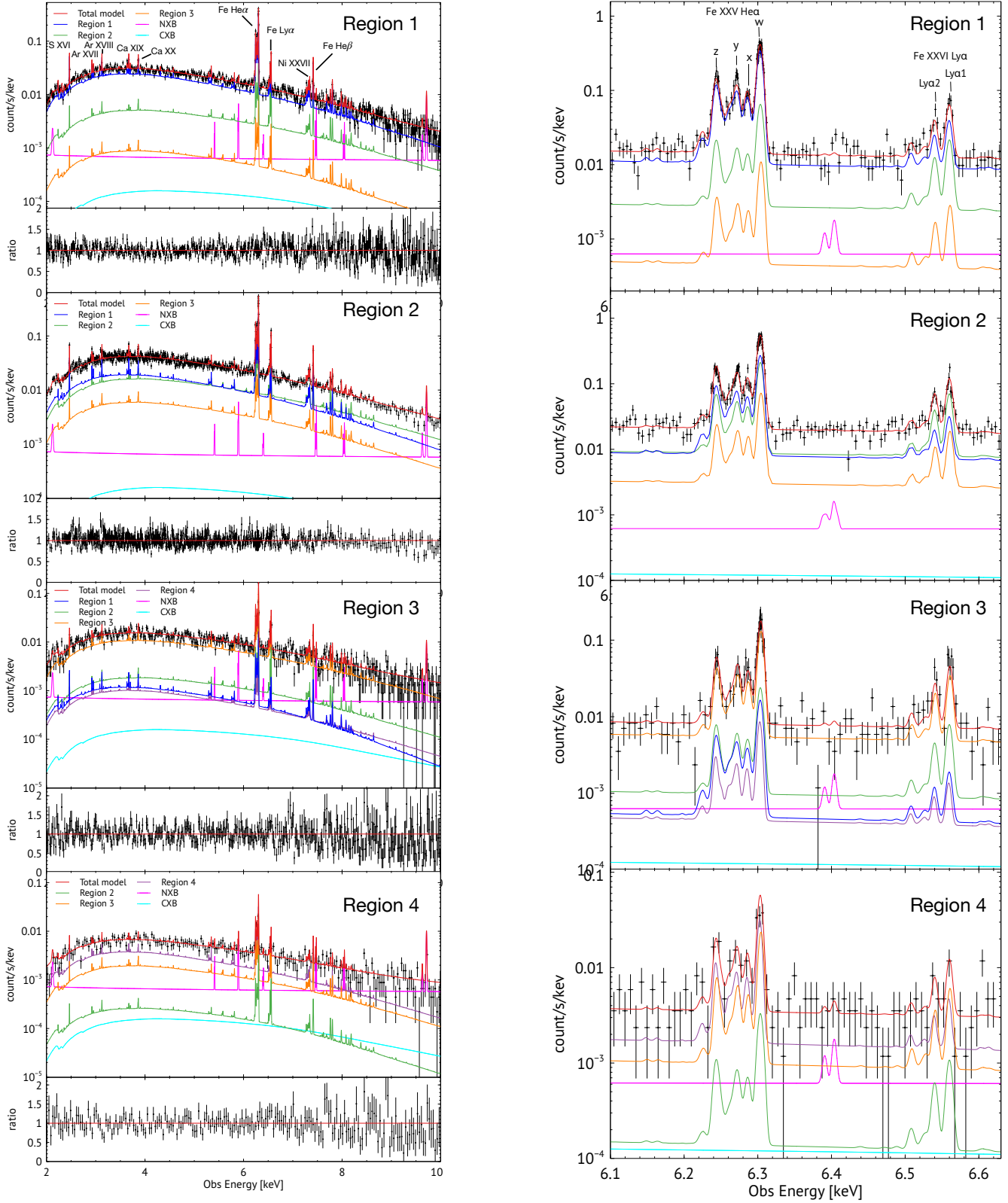
where  $z$  and  $z_{\text{BCG}}$  are the redshift of the hot ICM measured by XRISM and the redshift of the BCG, respectively.

Figure 5 shows the radial profile of the ICM bulk velocity in A1795 as a function of distance from the cluster center. Within the central  $1.5'$  (113 kpc), the bulk velocity is remarkably close to zero, suggesting no apparent motion between the BCG and local ICM. This result is in direct contrast to the “cooling-wake” scenario, in which the cool gas tail extending to the south is produced as the central cluster galaxy oscillates through the cluster core (A. C. Fabian et al. 2001). If it is the case, a measurable velocity offset between the BCG and ICM would be expected. Our results instead support the interpretation proposed by R. J. van Weeren et al. (2026), in which AGN-driven outflows uplift low-entropy gas from the cluster center to larger radii, where it eventually cools and condenses to form the observed tail.

### 4.2. Systematic uncertainties

Systematic uncertainties can alter the reliability of the measured ICM bulk velocity and velocity dispersion. The most important systematic effects for XRISM Resolve observations arise from calibration uncertainties in the energy scale (or “gain”) and the spectral line-spread function (LSF). The current in-flight gain calibration  $1\text{-}\sigma$  uncertainty is estimated to be  $\pm 0.3$  keV in the 5.4–9 keV band, and  $\pm 1$  keV below 5.4 keV, where high-fidelity calibration lines are not available on-orbit (M. E. Eckart et al. 2025). The bulk velocities reported in the previous section are primarily constrained by the He-like and H-like Fe K complexes at 6.2–6.6 keV, therefore we adopt a systematic bulk velocity uncertainty of  $0.3$  keV  $\approx 14$  km s $^{-1}$ . This is on the order of the lowest statistical error in the  $v_{\text{bulk}}$  measurements in Table 2.

The LSF calibration uncertainty arises from two sources: uncertainty in the intrinsic LSF width for a given pixel, and the spread of gain solutions across all pixels included in the analysis, which can produce an effective broadening in the combined spectrum. The former is estimated from results and methods in M. A. Leutenegger et al. (2025) to be  $\pm 0.16$  eV, quoting  $1\text{-}\sigma$  uncertainty in the LSF width. When added in quadrature with the measured line widths, this represents a systematic uncertainty of  $\lesssim 4$  km s $^{-1}$  in all velocity dispersions reported in this work, significantly smaller than the statistical errors. For the latter effect of pixel-to-pixel gain smearing, we follow the lead of A. Simionescu



**Figure 2.** Left panels: XRISM/Resolve sub-array counts spectra are shown along with the best-fit 1T models after accounting for Spatial-Spectral Mixing. In all four panels, the best-fit model components are folded through the relevant instrumental response and plotted as follows: red, blue, green, orange, purple, magenta, and cyan for the total model, region 1 ( $0-0.75'$ ), region 2 ( $0.75'-1.5'$ ), region 3 ( $1.5'-3'$ ), region 4 ( $3'-4.5'$ ), NXB, and CXB, respectively. Bottom panels in all four spectra represent ratios between data/model. Right panels: Same as left but zoomed into Fe xxv-He $\alpha$  and Fe xxvi-Ly $\alpha$  line complexes.

**Table 2.** Best-fit parameters from Resolve spectral fitting

Model	Radius	$kT$ (keV)	Abun (solar)	Redshift*	$\sigma_v$ (km/s)	$v_{\text{bulk}}^{\ddagger}$ (km/s)	norm <sup>†</sup> ( $10^{12} \text{ cm}^{-5}$ )	C-stat/d.o.f
1T	0 – 0.75'	$3.92 \pm 0.07$	$0.58 \pm 0.03$	$0.06308 \pm 0.00004$	$114 \pm 11$	$22 \pm 12$	$2.2 \pm 0.1$	17145/15999
	0.75' – 1.5'	$6.28 \pm 0.27$	$0.61 \pm 0.06$	$0.06302 \pm 0.00007$	$115 \pm 23$	$7 \pm 21$	$1.1 \pm 0.1$	17121/15999
	1.5' – 3'	$5.53 \pm 0.22$	$0.47 \pm 0.05$	$0.06289 \pm 0.00007$	$86 \pm 25$	$-32 \pm 21$	$1.9 \pm 0.1$	14122/15999
	3' – 4.5'	$4.23 \pm 0.37$	$0.28 \pm 0.06$	$0.06317 \pm 0.0002$	$68 \pm 39$	$47 \pm 60$	$1.2 \pm 0.1$	10594/15999
2T	0 – 0.75'	$2.72 \pm 0.67$	$0.63 \pm 0.03$	$0.06308 \pm 0.00004$	$187 \pm 60$	$22 \pm 12$	$0.7 \pm 0.3$	17138/15999
		$4.65 \pm 0.35$	– <sup>††</sup>	–	$93 \pm 24$	–	$1.5 \pm 0.5$	
	0.75' – 1.5'	$5.12 \pm 0.71$	$0.54 \pm 0.04$	$0.06303 \pm 0.00009$	$87 \pm 34$	$10 \pm 27$	$0.9 \pm 0.3$	17115/15999
		$6.81 \pm 1.22$	–	–	$175 \pm 70$	–	$0.4 \pm 0.2$	
	1.5' – 3'	$1.18 \pm 0.76$	$0.55 \pm 0.05$	$0.06289 \pm 0.00007$	–	$-32 \pm 21$	$0.4 \pm 0.3$	14117/15999
		$6.08 \pm 0.34$	–	–	$90 \pm 24$	–	$1.6 \pm 0.1$	
	3' – 4.5'	$4.30 \pm 0.38$	$0.29 \pm 0.06$	$0.06317 \pm 0.00017$	$63 \pm 30$	$47 \pm 51$	$1.2 \pm 0.1$	10588/15999
		–	–	–	–	–	–	–

\*: Redshift is corrected for solar system barycenter. <sup>‡</sup>: Only statistical fitting uncertainties are shown; BCG redshift uncertainty and the instrumental systematic gain uncertainty are not included. <sup>†</sup>: BAPEC normalizations correspond to the annuli shown in Figure 1. <sup>††</sup>: parameters are linked between two BAPEC temperature components for each region.

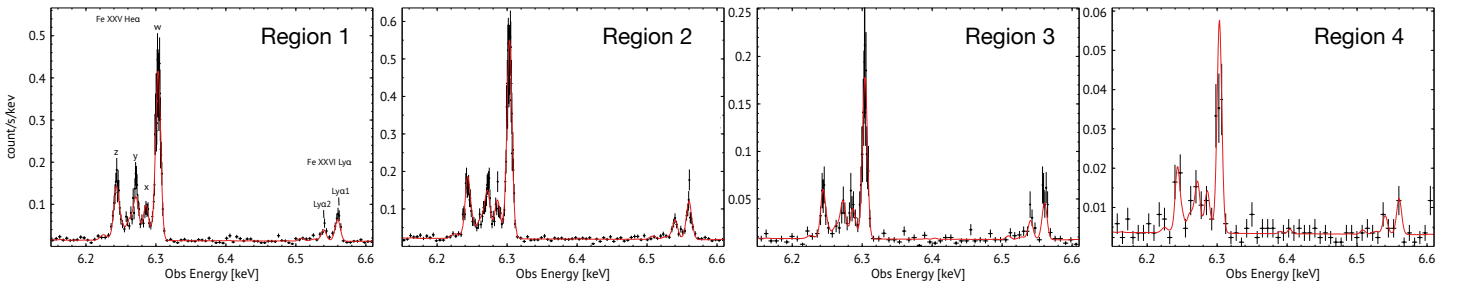


**Figure 3.** XRISM/Resolve sub-array counts spectra are shown together with the best-fit total 1T models, as in Figure 2, but with linear y-axes and zoomed in on the Fe-band region.

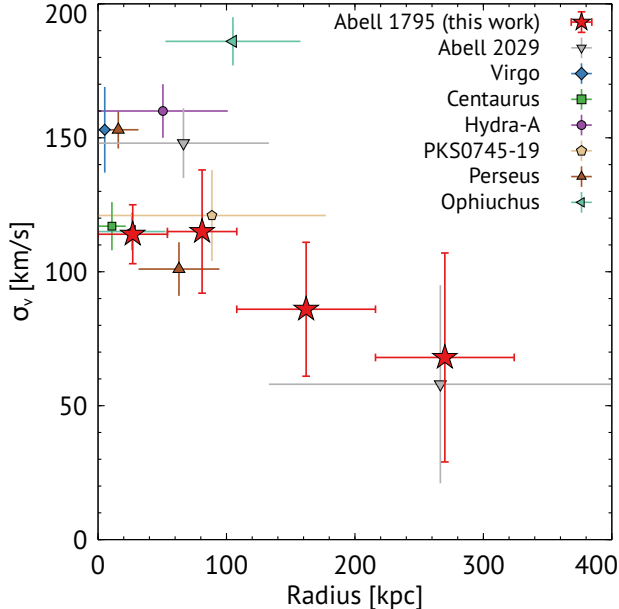


**Figure 4.** Radial profile of the line-of-sight velocity dispersion in A1795 (red star). Velocity dispersion measurements from other clusters are shown for comparison, including A2029 (XRISM Collaboration et al. 2025b; A. Sarkar et al. 2025b), Virgo (XRISM Collaboration et al. 2026), Centaurus (XRISM Collaboration et al. 2025c), Hydra A (T. Rose et al. 2025), PKS 0745–19 (K. Tanaka et al. 2026), Perseus (The Xrism Collaboration et al. 2026), and Ophiuchus (Y. Fujita et al. 2025).

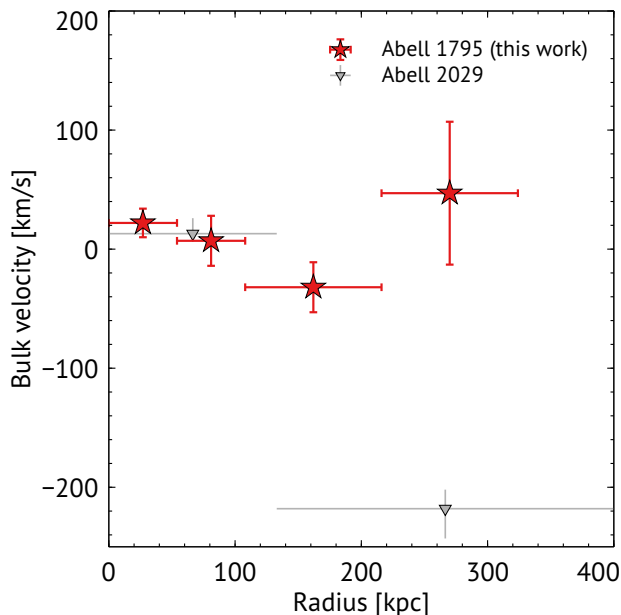


**Figure 5.** Bulk velocities in A1795 as a function of distance from the cluster center (red star). Grey inverted triangles indicate the bulk velocities measured in the A2029 cluster (XRISM Collaboration et al. 2025b; A. Sarkar et al. 2025b).

et al. (2026) and assume that this spread is the same as the overall gain uncertainty quoted above,  $\pm 0.3$  keV at 5.4–9 keV and  $\pm 1$  keV below 5.4 keV. This conservative assumption produces a systematic uncertainty of  $\lesssim 6$   $\text{km s}^{-1}$  for all reported velocity dispersions except those measured in the 2–4 keV band in Section 4.5, which have uncertainties of  $\sim 55$   $\text{km s}^{-1}$ . These systematic uncertainties due to energy-related calibration do not alter the conclusions in this work.

Additional sources of systematic uncertainty include point-spread-function calibration and the use of SSM; the level of the background; the energy range; the amount of spectral binning; the presence of multi-temperature ICM; the presence of resonant scattering; and the versions of software and atomic databases employed. Several of these effects are explored in the following sections. For the others, specifically SSM, background, binning, and software/atomic database versions, we point to the results from XRISM Collaboration et al. (2025b) and XRISM Collaboration et al. (2026), who study these effects in detail for Resolve galaxy cluster observations and find no significant impact on their results. The observations and velocity structure results presented here for A1795 are very similar to those studies, therefore we conclude that these other systematic uncertainties should not alter the conclusions from this work.

### 4.3. Non-thermal pressure support

We follow the procedure of XRISM Collaboration et al. (2025b) to infer the contribution of non-thermal pressure from the measured ICM velocity structure. The ratio of non-thermal pressure to the total pressure is estimated using

$$\frac{P_{\text{NT}}}{P_{\text{T}}} = \frac{\mathcal{M}_{3\text{D,eff}}^2}{\mathcal{M}_{3\text{D,eff}}^2 + \frac{3}{\gamma}}, \quad (2)$$

where  $\mathcal{M}_{3\text{D,eff}}$  denotes the effective three-dimensional Mach number, computed by combining the contributions from both the velocity dispersion and the bulk velocity components, as

$$\mathcal{M}_{3\text{D,eff}} = \frac{\sigma_{v,\text{eff}}}{c_s} = \frac{\sqrt{3\sigma_v^2 + v_{\text{bulk}}^2}}{c_s}, \quad (3)$$

where  $c_s$  is the sound speed, estimated as  $c_s = \sqrt{\frac{\gamma k_B T}{\mu m_p}}$ . Here,  $\gamma = 5/3$ ,  $k_B T$  is the measured X-ray temperature,  $\mu$  is the mean molecular weight, and  $m_p$  is the proton mass. We make two important assumptions in Eqs. 2 and 3. First, we assume that all non-thermal pressure arises from turbulence, and we ignore other possible contributions like magnetic fields and cosmic rays (e.g., S.

Ettori & D. Eckert 2022). Second, we assume the measured velocity dispersion is due fully to isotropic turbulence, and we include the line-of-sight bulk velocity in our estimate of the three-dimensional Mach number. These assumptions are consistent with recent XRISM studies (XRISM Collaboration et al. 2025b, e.g.). We note that  $\mathcal{M}_{3D,eff}$  ranges from 0.1 to 0.2 in the regions of our observation, indicating sub-sonic ICM motions.

Figure 6 shows the radial profile of the derived non-thermal-to-total pressure ratio,  $P_{NT}/P_T$ , in A1795. Beyond  $\sim 200$  kpc from the cluster center, A1795 exhibits a remarkably low non-thermal pressure fraction ( $\sim 0.6\%$ ) compared to other clusters observed with XRISM, indicating a quiescent ICM just outside the cluster center. This is the lowest non-thermal pressure fraction so far recorded in a cluster as measured by XRISM far (at  $\sim 300$  kpc) from cluster core. XRISM Collaboration et al. (2025b) found a  $P_{NT}/P_T \sim 0.9 \pm 0.7\%$  near  $R_{2500}$  of A2029, claiming such low non-thermal pressure is rare for a relaxed cluster and does not have a counterpart in the simulated cluster sample (XRISM Collaboration et al. 2025e). Our measurements of  $P_{NT}/P_T$  in A1795 suggest that this is not rare. The non-thermal pressure may have a decreasing trend for relaxed cool-core clusters reaching below 1% near  $R_{2500}$ . Within 200 kpc, the non-thermal pressure fraction in A1795 ( $\sim 1\text{--}2\%$ ) is comparable to that measured in A2029 (XRISM Collaboration et al. 2025a,b), Perseus (Hitomi Collaboration et al. 2016b), and PKS0745-19 (K. Tanaka et al. 2026).

We compare our results with that of previous indirect velocity measurements. A. Heinrich et al. (2024) examined X-ray surface brightness fluctuations within  $R_{2500}$  for a sample of luminous galaxy clusters observed with Chandra. They derived power spectra of density fluctuations and translated these into velocity power spectra under the assumptions of proportionality between two, adopting a calibration of the proportionality factor for clusters in different dynamical states from I. Zhuravleva et al. (2023). This analysis derived  $P_{NT}/P_T$  values of  $\sim 0.7\text{--}7\%$  within the central  $R_{2500}$  of clusters similar to A1795. We measure  $P_{NT}/P_T$  between  $2.1 \pm 0.2\%$  and  $0.6 \pm 0.4\%$  within  $0\text{--}0.5 R_{2500}$  ( $0\text{--}320$  kpc) of A1795's center, with a median value of  $\sim 1\%$ . These results are very close to the  $P_{NT}/P_T$  derived from indirect measurements.

If the non-thermal pressure fraction in A1795 follows the decreasing trend up to  $R_{2500}$  (as shown in Figure 6), it does not significantly bias cluster mass measurements. However, our conclusion relies on  $P_{NT}/P_T$  measurements along one azimuthal direction. Simulations of cluster cores with prominent gas sloshing suggest that ICM gas velocities can be highly anisotropic,

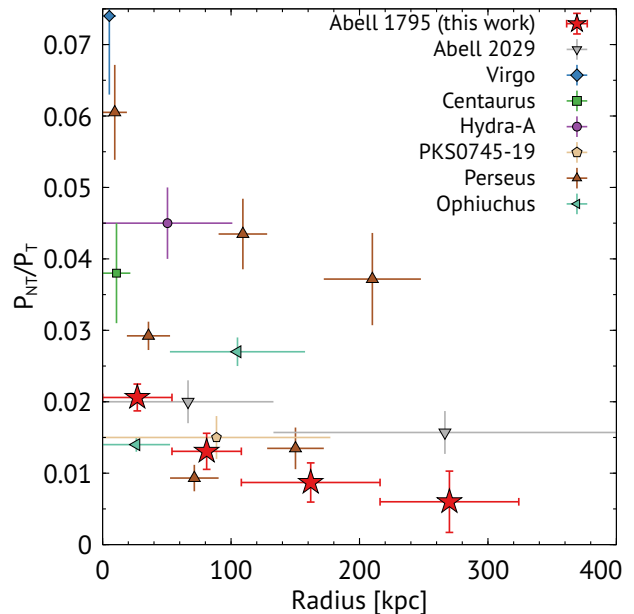


**Figure 6.** Radial profile of the non-thermal pressure fraction in A1795 measured from the cluster center (red star). Other data points show the non-thermal pressure fractions measured in other clusters, as indicated in the legend.

and assuming isotropy can lead to underestimation of the overall gas velocity (Y. Fujita et al. 2004). The ICM of A1795 is remarkably smooth just outside the central  $\sim 100$  kpc, showing no prominent X-ray substructures, implying low non-thermal pressure at larger radii in all directions. However, such confirmation needs future observations sampling multiple directions of A1795.

#### 4.4. Turbulent Heating

A phenomenological turbulent heating model was fit to the X-ray luminosity profile of the cluster, where the heating power:

$$P_{\text{turb}} \simeq \frac{3}{2} M(r) \frac{\sigma_v^3}{l} \quad (4)$$

is assumed to balance cooling from the emission of X-rays.  $M(r)$  is the atmospheric gas mass subtended by the image within the radius that the velocity dispersion  $\sigma_v$  is measured by XRISM. The gas mass  $M(r)$  and X-ray luminosity  $L_x(r)$  are taken from the catalog of cluster thermodynamic profiles discussed by F. A. Pulido et al. (2018) and M. T. Hogan et al. (2017). The turbulent dissipation timescale is assumed to be  $\sim l/\sigma_v$ . The energy injection scale  $l$  cannot be measured by XRISM but is expected to be on the order of the X-ray bubbles and jets imparting energy into the X-ray atmosphere. Those scales are typically a few to a few tens of kpc, which is below XRISM's spatial resolution. In general,  $\sigma_v$  and  $l$  must be measured on the same scales. Instead,

Eq. 4 is used to evaluate the radial range of  $l$  required to instantaneously balance radiative losses, constrained by the observed velocity dispersion.

If turbulent dissipation is the primary mechanism offsetting the cooling flow, it must operate over the cooling radius  $\sim 130$  kpc (D. A. Rafferty et al. 2006). The inner two velocity dispersion measurements roughly encompass this region. The inner 60 kpc assumes  $\sigma_v = 114$  km s $^{-1}$  and from 60 kpc to the cooling radius  $\sigma_v = 115$  km s $^{-1}$  is assumed. Anchored by the measured velocity dispersions,  $l$  was allowed to vary with radius so that at all radii  $P_{\text{turb}} \simeq L_x(r)$ . A radial trend in  $l$  lying between  $\simeq 2$  kpc in the inner 25 kpc rising to  $\simeq 15$  kpc at the cooling radius would be required to fit the luminosity profile. This equilibrium model between energy injection, presumably by the jets and bubbles, and heating through a turbulent cascade in turn implies a timescale of  $\tau \sim l/\sigma_v \sim 2 \times 10^7$  yr in the inner 25 kpc and rising to  $\sim 10^8$  yr at the cooling radius. A complete description of this approach is given in T. Rose et al. (2025) and B. R. McNamara et al. (2026).

If the turbulence energy propagates at  $v \sim 114$  km/s, it would take  $\sim 1.1 \times 10^9$  yr to reach the cooling radius, roughly 10 times longer than the time scale needed for turbulent energy dissipation as heat required to offset cooling. However, turbulence diffuses much more slowly than the turbulent eddy speed (McNamara et al., in preparation), which implies turbulent energy is dissipated locally, well before it can be transported to larger radii. Turbulence is probably an inefficient mechanism for redistributing AGN injected energy (via jets/bubbles) throughout the cooling volume. Instead, these results support a scenario in which heating must be spatially distributed, with energy deposited in situ across the cooling region. For turbulence to offset cooling entirely, it must propagate at a speed of  $\sim 1300$  km s $^{-1}$ , assuming cooling time varies linearly with radius, which is roughly a factor of 10 higher than  $\sigma_v$ .

Our measurements indicate turbulent heating alone struggles to offset cooling in A1795’s core. Similar conclusions have been drawn for Hydra-A, Virgo, and Ophiuchus in previous XRISM studies, suggesting additional heating channels, such as weak shocks and cosmic ray, are required (e.g., XRISM Collaboration et al. 2026; Y. Fujita et al. 2025; T. Rose et al. 2025).

#### 4.5. Multi-phase ICM

We examine the presence of multiphase gas in A1795 by fitting the Resolve spectrum from each region with a two-temperature collisional ionization equilibrium (2T CIE) model, BVAPEC + BVAPEC. We allow the temperature ( $kT$ ), velocity dispersion ( $\sigma_v$ ), and normalization of

each component to vary independently, while accounting for SSM using the same fitting procedure described in Section 3. The best-fit parameters from the 2T fits for each region are listed in Table 2.

Within the central 0.75’ ( $\sim 50$  kpc), we detect two distinct temperature components: a cooler component at  $\sim 2.7$  keV and a hotter component at  $\sim 4.6$  keV. This is consistent with the results of T. Tamura et al. (2001), who found similar ICM temperatures within the central 2’ using XMM-Newton. The cooler component shows a LOS velocity dispersion that is higher by  $\Delta\sigma_v \approx 90$  km/s compared to the hotter component. A similarly higher velocity dispersion is also observed in the 0.75’–1.5’ ( $\sim 50$ –103 kpc) region, with  $\Delta\sigma_v = 88$  km/s, although the two components have consistent temperatures. These results indicate the presence of multiphase gas in the central regions of A1795. In the 1.5’–3’ (103–206 kpc) region, we obtain a cooler temperature component of 1.2 keV; however, the velocity dispersions of the individual components cannot be constrained. For the 3’–4.5’ (206–310 kpc) region, the second temperature component is not well constrained when left free and is therefore tied to that of the first component. In both outer annuli, the jointly fitted  $\sigma_v$  values are consistent with that of obtained from the 1T fit.

To confirm the presence of multi-phase gas at the A1795 core, we re-fit the Resolve spectra from the 0 – 0.75’ and 0.75’ – 1.5’ annuli in two separate energy bins: 2–4 keV and 6–7 keV. The motivation behind this is that the 2–4 keV energy band is more sensitive to cooler gas, while the 6–7 keV band traces hotter gas, in both cases compared to broadband 2–10 keV fitting. The resulting best-fit parameters for both regions are listed in Table 3. Within the central 0.75’, the 2–4 keV band yields significantly lower temperatures and metallicities than those obtained from the 6–7 keV band. The cooler gas component also has a higher LOS velocity dispersion than the hotter component. In the 0.75’ – 1.5’ region, both energy bands yield consistent temperatures and metallicities. Although we are able to constrain  $\sigma_v$  of  $\sim 100$  km/s from the 6–7 keV fit, we cannot constrain  $\sigma_v$  from the 2–4 keV fit due to low statistical quality, however a  $1\sigma$  upper limit of 200 km/s is obtained.

The split-band results are consistent with the best-fit parameters obtained from the 2T broadband fitting for both regions. These results suggest the presence of multiphase gas in the central region of A1795, in line with previous Chandra and GMRT observations (G. Kokotanekov et al. 2018b). The central 80 kpc of A1795 is morphologically disturbed, showing multiple X-ray cavities, surface brightness edges, and a cool gas tail extending to the south, as shown in Figure 1.

These features result from multiple episodes of mechanical feedback from the central AGN, which shock-heat the ICM, inject turbulence (M. Gaspari et al. 2012; B. R. McNamara & P. E. J. Nulsen 2012), and uplift cool gas from the center (R. J. van Weeren et al. 2026), giving rise to a multiphase ICM in the core of A1795.

#### 4.6. Resonant Scattering

Line intensities of optically thick transitions in the observed X-ray spectra can be reduced by resonant scattering, in which line photons are absorbed and re-emitted in different directions, effectively scattering photons out of the line of sight and suppressing the observed line strength (e.g., E. Churazov et al. 2004; J. S. Sanders & A. C. Fabian 2006; D. Nelson et al. 2023). Resonant scattering effects are expected to be strongest in the central regions of clusters, where the gas density is highest. Because the Resolve gate valve was closed during the observations, the only potentially optically thick line resolved in A1795 with XRISM at high significance is the Fe xxv  $w$  line at 6.7 keV. We estimate the degree of resonant line suppression in the central region of A1795 by fitting Resolve full-array spectra extracted from the cluster core with a two-temperature RSAPEC model (P. Chakraborty et al. 2023) in XSPEC. The RSAPEC model provides a simple, single-step, and computationally efficient treatment of resonant scattering, and serves as an alternative to the BAPEC model for modeling spectra from collisionally ionized plasma. Figure 7 compares the best-fit collisional ionization equilibrium (CIE) models before and after accounting for resonant scattering, together with the observed Resolve spectra from the central region of A1795.

For both temperature components, we allow the temperature ( $kT$ ), abundance, redshift, and normalization to vary freely, while the line-of-sight column density (in the RSAPEC model) is tied between the two components. Because resonant scattering suppression depends sensitively on velocity broadening, the velocity dispersion parameters,  $\sigma_v$ , are also allowed to vary independently for both components during the fitting. Table 4 summarizes the best-fit parameters obtained for the two-temperature models. For the RSAPEC fit, we find best-fit temperatures of  $3.86 \pm 0.19$  keV and  $6.61 \pm 0.59$  keV, with corresponding velocity dispersions of  $98 \pm 16$  km s $^{-1}$  and  $130 \pm 17$  km s $^{-1}$ . These values are consistent with those derived from the two-temperature BAPEC model, which does not account for resonant scattering effects. By comparing the Fe xxv  $w$  line flux predicted by the best-fit BAPEC model with that from the RSAPEC fit, we infer a resonant scattering suppression factor of  $\sim 14\%$ . As expected, the suppression is strongest in the cluster

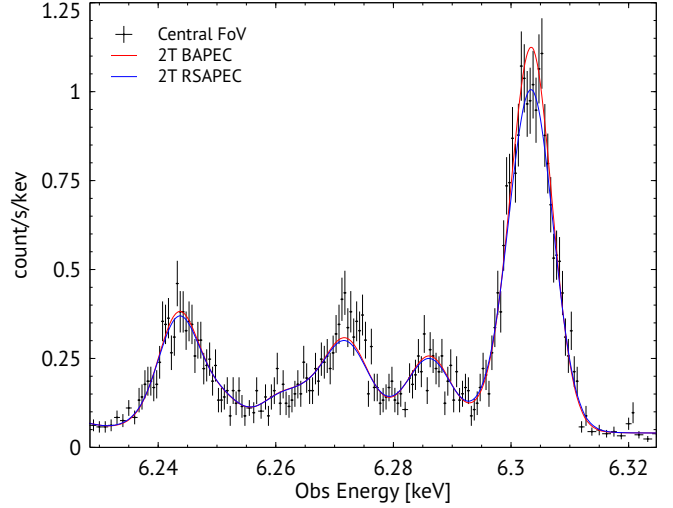


**Figure 7.** Resolve spectrum from the entire central pointing (black data points) fitted with single temperature velocity broadened CIE model without accounting for resonant scattering (BAPEC; red) and with accounting resonant scattering (RSAPEC; blue). Line flux of optically thick Fe xxv  $w$  line is suppressed by a factor of  $\sim 14\%$ .

core. Resonant scattering effects can be even more pronounced in lower-energy lines in cooler clusters such as A1795; however, Resolve lacks sensitivity below 2 keV due to the loss of low-energy response. Future X-ray microcalorimeter missions, such as NewAthena, will therefore be essential for detailed studies of resonant scattering in galaxy clusters. We are unable to constrain resonant scattering in the northern region because of the low ICM surface brightness, and deeper observations will be required to improve these constraints.

#### 4.7. Fe xxv $y$ line anomaly

We identify a significant positive residual in the Fe xxv He $\alpha$   $y$  intercombination line at 6.668 keV in the Resolve spectra of A1795 when fitted with a two-temperature collisional ionization equilibrium model that includes resonant scattering effects (2T RSAPEC). Figure 8 illustrates this anomaly in the full-array Resolve spectrum extracted from the central region of A1795. Such enhanced observed flux in the Fe xxv He $\alpha$   $y$  line, compared to that predicted by the best-fit model, has also been reported in other clusters, including Ophiuchus (Y. Fujita et al. 2025) and Abell 2029 (XRISM Collaboration et al. 2025a). We investigate possible origins of this line anomaly in A1795. In this work, we limit our analysis to the central pointing, where the spectral quality is significantly higher than in the northern pointing. We find that even after accounting for resonant scattering and fitting with a 2T CIE model, a substantial residual in the  $y$  line persists, as shown in Figure 8.

**Table 3.** Best-fit parameters for central two regions fitted in two spectra ranges: 2–4 keV and 6–7 keV

Radius	$kT$ (keV)	Abun (solar)	Redshift	$\sigma_v$ (km/s)	$v_{\text{bulk}}$ (km/s)	norm ( $10^{12} \text{ cm}^{-5}$ )
Range: 2–4 keV						
0 – 0.75'	$3.40 \pm 0.20$	$0.47 \pm 0.11$	$0.06279 \pm 0.00022$	$189 \pm 61$	$-60 \pm 66$	$2.1 \pm 0.1$
0.75' – 1.5'	$4.98 \pm 0.47$	$0.38 \pm 0.17$	$0.063335 \pm 0.00045$	$< 200$	$98 \pm 135$	$1.8 \pm 0.1$
Range: 6–7 keV						
0 – 0.75'	$4.62 \pm 0.16$	$0.68 \pm 0.05$	$0.06311 \pm 0.00004$	$115 \pm 12$	$30 \pm 12$	$1.8 \pm 0.1$
0.75' – 1.5'	$5.57 \pm 0.23$	$0.47 \pm 0.05$	$0.06295 \pm 0.00006$	$107 \pm 19$	$-15 \pm 18$	$1.7 \pm 0.1$

**Table 4.** Best-fit parameters for full-array central FoV fitted with 2T BAPEC and RSAPEC models within 2–10 keV.

Model	$kT$ (keV)	Abun (solar)	Redshift	$\sigma_v$ (km/s)	Column density ( $10^{22} \text{ cm}^{-2}$ )	norm ( $10^{12} \text{ cm}^{-5}$ )
BAPEC	$4.62 \pm 0.16$	$0.68 \pm 0.05$	$0.06311 \pm 0.00004$	$115 \pm 12$	–	$1.8 \pm 0.1$
	$5.57 \pm 0.23$	$0.47 \pm 0.05$	$0.06295 \pm 0.00006$	$107 \pm 19$	–	$1.7 \pm 0.1$
RSAPEC	$3.86 \pm 0.19$	$0.59 \pm 0.04$	$0.06303 \pm 0.00006$	$98 \pm 16$	$0.2 \pm 0.1$	$2.4 \pm 0.4$
	$6.61 \pm 0.59$	$0.59 \pm 0.05$	$0.062304 \pm 0.00006$	$130 \pm 17$	– <sup>†</sup>	$1.6 \pm 0.4$

<sup>†</sup>parameters are linked between the two temperature components

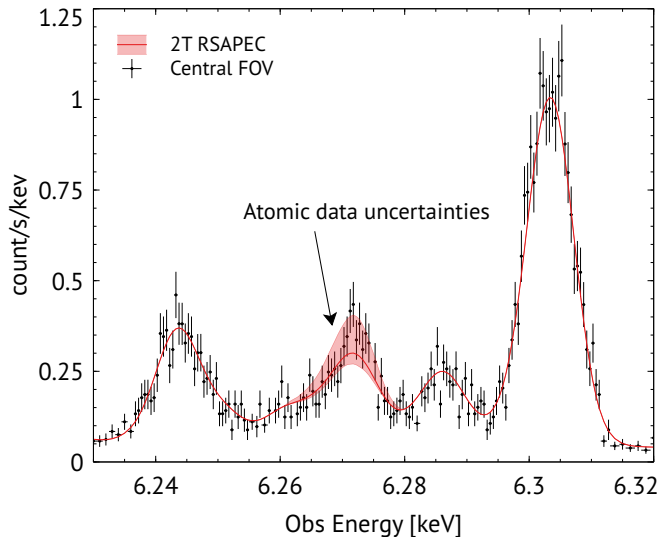


**Figure 8.** Resolve spectrum extracted from the central FOV (black data), as shown in Figure 1, fitted with a two-temperature CIE model (red curve) accounting for resonant scattering of optically thick lines. Shaded region shows the variation of Fe XXV-He $\alpha$   $\gamma$ -line emissivity due to atomic data uncertainties in the transition probability and collision strength.

P. Chakraborty et al. (2024) demonstrated that the physical interpretation of X-ray spectra depends critically on the accuracy of the atomic data used in spectral synthesis codes (see also Hitomi Collaboration et al. 2018b). For collisionally ionized ICM plasma, spectral line emissivities are particularly sensitive to uncertainties in the Einstein  $A$  coefficients and the colli-

sional rate coefficients, which represent the Maxwellian-averaged collision cross sections ( $q$  values). We investigate whether the excess  $\gamma$ -line flux residual observed in A1795 can be explained by uncertainties in the underlying atomic data. To do this, we use the `variableapec` module within `pyatomdb` (A. R. Foster & K. Heuer 2020), as described in P. Chakraborty et al. (2024). The `variableapec` module allows individual atomic parameters, such as Einstein  $A$  coefficients and collisional rate coefficients, to be varied independently and computes the resulting changes in individual line emissivities. The modified emissivities are then incorporated into XSPEC by updating the `apecv3.1.2_line.fits` file.

To isolate the impact of atomic data uncertainties on the  $\gamma$ -line emissivity, we vary only the Einstein  $A$  coefficients and collisional rate coefficients associated with the  $\gamma$  transition. Based on Table 3 of Hitomi Collaboration et al. (2018b) and Table 1 of P. Chakraborty et al. (2024), we adopt uncertainties of 14% in the Einstein  $A$  coefficients and 18% in the collisional rate coefficients for the  $\gamma$ -line. We then use `variableapec` to quantify the resulting changes in the  $\gamma$ -line intensity using a Markov Chain Monte Carlo chain with 1000 realizations. Figure 8 shows the variation in the  $\gamma$ -line emissivity as the atomic parameters are varied within these uncertainty ranges, with the modified emissivities propagated through XSPEC. We find that some sets of Einstein  $A$  coefficients and collisional rate coefficients increases the predicted  $\gamma$ -line emissivity (shade region in Figure 8), thereby reducing the discrepancy between

the model and the observed spectrum. However, we caution that this analysis provides only suggestive evidence that uncertainties in the atomic data may contribute to the observed excess  $y$ -line flux, in combination with the physical properties of the ICM. Additional high-quality Resolve cluster spectra will be required to robustly determine the origin of the enhanced  $y$ -line emission.

## 5. SUMMARY

We present a total of  $\sim 338$  ks XRISM Resolve observations of the A1795 galaxy cluster. Our main results are summarized below.

- We split two consecutive Resolve pointings (central and North) into four regions and extracted spectra from each region. Single-temperature fits reveal a gradient in line-of-sight velocity dispersion, decreasing from  $114 \text{ km s}^{-1}$  to  $68 \text{ km s}^{-1}$  from the central to the outermost region at  $\sim 330$  kpc.
- The measured bulk velocities in the two central regions are low:  $-4$  and  $-10 \text{ km s}^{-1}$ , suggesting no significant relative motion between the BCG and ICM. Because the innermost region includes the cool gas tail extending to south, such low bulk velocity directly contradict the “cooling-wake” scenario for the origin of the tail. Instead, it supports the AGN-uplift origin.
- The non-thermal pressure fraction shows a decreasing trend with radius, with  $P_{\text{NT}}/P_{\text{T}} = 0.019 \pm 0.002$  in the core, declining to a remarkably low value of  $0.006 \pm 0.004$  at 330 kpc from the cluster center. Such low non-thermal pressure indicates that the ICM in the northern region of A1795 is largely quiescent.
- Our measurements suggest turbulent heating alone struggles to balance the cooling within the

cooling radius ( $\sim 130$ ) of A1795. It supports a scenario in which heating must be spatially distributed, with energy deposited in situ across the cooling region.

- We have identified two gas phases with  $\Delta\sigma_v \approx 94 \text{ km s}^{-1}$  and  $88 \text{ km s}^{-1}$  within the central  $< 0.75'$  and  $0.75' - 1.5'$  regions, respectively, based on a two-temperature fit and split energy band fit (2–4 keV and 6–7 keV). These results strongly suggest the presence of multiphase gas in the center of A1795.
- A  $\sim 14\%$  suppression of the optically-thick Fe XXV  $-w$  line-flux in the central region of A1795 has been detected, suggesting resonant scattering of line-of-sight X-ray photons from the cluster core to larger radii.
- We have identified a significant positive residual in the observed flux of the Fe XXV  $-y$  line at 6.668 keV when fitted with CIE models. Similar enhancements have been reported in other clusters, such as Ophiuchus and A2029. We find that including atomic data uncertainties in the Einstein  $A$  coefficient and collisional rate of  $y$ -line reduces the discrepancy between the observation and the models. Our analysis provides a suggestive evidence that underlying uncertainties in atomic data may (partially) contribute to the observed excess  $y$ -line flux.

## ACKNOWLEDGEMENT

We thank the anonymous referee for their helpful comments. We gratefully acknowledge the dedicated efforts of the many engineers and scientists whose hard work over the years made the XRISM mission possible. AS acknowledges support from NASA grant 80NSSC26K0916 and EDM acknowledges support from NASA grants 80NSSC25K7538 and 80NSSC24K0678.

## REFERENCES

- Arnaud, K. A. 1996, in *Astronomical Society of the Pacific Conference Series*, Vol. 101, *Astronomical Data Analysis Software and Systems V*, ed. G. H. Jacoby & J. Barnes, 17
- Bautz, M. W., Miller, E. D., Sanders, J. S., et al. 2009, *PASJ*, 61, 1117, doi: [10.1093/pasj/61.5.1117](https://doi.org/10.1093/pasj/61.5.1117)
- Cash, W. 1979, *ApJ*, 228, 939, doi: [10.1086/156922](https://doi.org/10.1086/156922)
- Center, N. H. E. A. S. A. R. 2014, *HEAsoft: Unified Release of FTOOLS and XANADU*, *Astrophysics Source Code Library*, record ascl:1408.004 <http://ascl.net/1408.004>
- Chakraborty, P., Foster, A., Smith, R., Brickhouse, N., & Raymond, J. 2023, *ApJ*, 959, 126, doi: [10.3847/1538-4357/acfe10](https://doi.org/10.3847/1538-4357/acfe10)
- Chakraborty, P., Hemmer, R., Foster, A. R., et al. 2024, *ApJ*, 962, 192, doi: [10.3847/1538-4357/ad17be](https://doi.org/10.3847/1538-4357/ad17be)
- Churazov, E., Forman, W., Jones, C., Sunyaev, R., & Böhringer, H. 2004, *MNRAS*, 347, 29, doi: [10.1111/j.1365-2966.2004.07201.x](https://doi.org/10.1111/j.1365-2966.2004.07201.x)

- Eckart, M. E., Brown, G. V., Chiao, M. P., et al. 2025, *Journal of Astronomical Telescopes, Instruments, and Systems*, 11, 042018, doi: [10.1117/1.JATIS.11.4.042018](https://doi.org/10.1117/1.JATIS.11.4.042018)
- Ehlert, S., McDonald, M., David, L. P., Miller, E. D., & Bautz, M. W. 2015, *ApJ*, 799, 174, doi: [10.1088/0004-637X/799/2/174](https://doi.org/10.1088/0004-637X/799/2/174)
- Ettori, S., & Eckert, D. 2022, *A&A*, 657, L1, doi: [10.1051/0004-6361/202142638](https://doi.org/10.1051/0004-6361/202142638)
- Fabian, A. C., Sanders, J. S., Ettori, S., et al. 2001, *MNRAS*, 321, L33, doi: [10.1046/j.1365-8711.2001.04243.x](https://doi.org/10.1046/j.1365-8711.2001.04243.x)
- Foster, A. R., & Heuer, K. 2020, *Atoms*, 8, doi: [10.3390/atoms8030049](https://doi.org/10.3390/atoms8030049)
- Fujita, Y., Fukushima, K., Sato, K., Fukazawa, Y., & Kondo, M. 2025, *PASJ*, 77, S270, doi: [10.1093/pasj/psaf089](https://doi.org/10.1093/pasj/psaf089)
- Fujita, Y., Matsumoto, T., & Wada, K. 2004, *ApJL*, 612, L9, doi: [10.1086/424483](https://doi.org/10.1086/424483)
- Gaspari, M., Ruszkowski, M., & Sharma, P. 2012, *ApJ*, 746, 94, doi: [10.1088/0004-637X/746/1/94](https://doi.org/10.1088/0004-637X/746/1/94)
- Heinrich, A., Zhuravleva, I., Zhang, C., et al. 2024, *MNRAS*, 528, 7274, doi: [10.1093/mnras/stae208](https://doi.org/10.1093/mnras/stae208)
- HI4PI Collaboration, Ben Bekhti, N., Flöer, L., et al. 2016, *A&A*, 594, A116, doi: [10.1051/0004-6361/201629178](https://doi.org/10.1051/0004-6361/201629178)
- Hitomi Collaboration, Aharonian, F., Akamatsu, H., et al. 2016a, *Nature*, 535, 117, doi: [10.1038/nature18627](https://doi.org/10.1038/nature18627)
- Hitomi Collaboration, Aharonian, F., Akamatsu, H., et al. 2016b, *Nature*, 535, 117, doi: [10.1038/nature18627](https://doi.org/10.1038/nature18627)
- Hitomi Collaboration, Aharonian, F., Akamatsu, H., et al. 2018a, *PASJ*, 70, 9, doi: [10.1093/pasj/psx138](https://doi.org/10.1093/pasj/psx138)
- Hitomi Collaboration, Aharonian, F., Akamatsu, H., et al. 2018b, *PASJ*, 70, 12, doi: [10.1093/pasj/psx156](https://doi.org/10.1093/pasj/psx156)
- Hogan, M. T., McNamara, B. R., Pulido, F. A., et al. 2017, *ApJ*, 851, 66, doi: [10.3847/1538-4357/aa9af3](https://doi.org/10.3847/1538-4357/aa9af3)
- Kelley, R. L., Ishisaki, Y., Costantini, E., et al. 2025, *Journal of Astronomical Telescopes, Instruments, and Systems*, 11, 042026
- Kokotanekov, G., Wise, M. W., de Vries, M., & Intema, H. T. 2018a, *A&A*, 618, A152, doi: [10.1051/0004-6361/201833222](https://doi.org/10.1051/0004-6361/201833222)
- Kokotanekov, G., Wise, M. W., de Vries, M., & Intema, H. T. 2018b, *A&A*, 618, A152, doi: [10.1051/0004-6361/201833222](https://doi.org/10.1051/0004-6361/201833222)
- Leutenegger, M. A., Brown, G. V., Chiao, M. P., et al. 2025, *Journal of Astronomical Telescopes, Instruments, and Systems*, 11, 042024, doi: [10.1117/1.JATIS.11.4.042024](https://doi.org/10.1117/1.JATIS.11.4.042024)
- Lodders, K., & Palme, H. 2009, *Meteoritics and Planetary Science Supplement*, 72, 5154
- Markevitch, M., Vikhlinin, A., & Mazzotta, P. 2001, *ApJL*, 562, L153, doi: [10.1086/337973](https://doi.org/10.1086/337973)
- McDonald, M., & Veilleux, S. 2009, *ApJL*, 703, L172, doi: [10.1088/0004-637X/703/2/L172](https://doi.org/10.1088/0004-637X/703/2/L172)
- McNamara, B. R., Fabian, A. C., Russell, H. R., et al. 2026, arXiv e-prints, arXiv:2604.19607, doi: [10.48550/arXiv.2604.19607](https://doi.org/10.48550/arXiv.2604.19607)
- McNamara, B. R., & Nulsen, P. E. J. 2012, *New Journal of Physics*, 14, 055023, doi: [10.1088/1367-2630/14/5/055023](https://doi.org/10.1088/1367-2630/14/5/055023)
- Nelson, D., Byrohl, C., Ogorzalek, A., et al. 2023, *MNRAS*, 522, 3665, doi: [10.1093/mnras/stad1195](https://doi.org/10.1093/mnras/stad1195)
- Omiya, Y., Ichinohe, Y., Nakazawa, K., et al. 2026, *ApJL*, 996, L15, doi: [10.3847/2041-8213/ae2a28](https://doi.org/10.3847/2041-8213/ae2a28)
- Pulido, F. A., McNamara, B. R., Edge, A. C., et al. 2018, *ApJ*, 853, 177, doi: [10.3847/1538-4357/aaa54b](https://doi.org/10.3847/1538-4357/aaa54b)
- Rafferty, D. A., McNamara, B. R., Nulsen, P. E. J., & Wise, M. W. 2006, *ApJ*, 652, 216, doi: [10.1086/507672](https://doi.org/10.1086/507672)
- Rose, T., McNamara, B. R., Meunier, J., et al. 2025, *ApJ*, 990, 42, doi: [10.3847/1538-4357/adf32d](https://doi.org/10.3847/1538-4357/adf32d)
- Russell, H. R., McNamara, B. R., Fabian, A. C., et al. 2017a, *MNRAS*, 472, 4024, doi: [10.1093/mnras/stx2255](https://doi.org/10.1093/mnras/stx2255)
- Russell, H. R., McNamara, B. R., Fabian, A. C., et al. 2017b, *MNRAS*, 472, 4024, doi: [10.1093/mnras/stx2255](https://doi.org/10.1093/mnras/stx2255)
- Sanders, J. S., & Fabian, A. C. 2006, *MNRAS*, 370, 63, doi: [10.1111/j.1365-2966.2006.10497.x](https://doi.org/10.1111/j.1365-2966.2006.10497.x)
- Sanders, J. S., & Fabian, A. C. 2007, *MNRAS*, 381, 1381, doi: [10.1111/j.1365-2966.2007.12347.x](https://doi.org/10.1111/j.1365-2966.2007.12347.x)
- Sanders, J. S., Fabian, A. C., Russell, H. R., Walker, S. A., & Blundell, K. M. 2016, *MNRAS*, 460, 1898, doi: [10.1093/mnras/stw1119](https://doi.org/10.1093/mnras/stw1119)
- Sarkar, A., Randall, S., Su, Y., et al. 2022, *ApJL*, 935, L23, doi: [10.3847/2041-8213/ac86d4](https://doi.org/10.3847/2041-8213/ac86d4)
- Sarkar, A., Randall, S., Su, Y., et al. 2023, *ApJ*, 944, 132, doi: [10.3847/1538-4357/acaef9](https://doi.org/10.3847/1538-4357/acaef9)
- Sarkar, A., McDonald, M., Bleem, L., et al. 2025a, *ApJL*, 984, L63, doi: [10.3847/2041-8213/adc676](https://doi.org/10.3847/2041-8213/adc676)
- Sarkar, A., Miller, E., Ota, N., et al. 2025b, *PASJ*, 77, S254, doi: [10.1093/pasj/psaf093](https://doi.org/10.1093/pasj/psaf093)
- Simionescu, A., Zuhone, J., Zhuravleva, I., et al. 2019, *SSRv*, 215, 24, doi: [10.1007/s11214-019-0590-1](https://doi.org/10.1007/s11214-019-0590-1)
- Simionescu, A., Kilbourne, C., Russell, H. R., et al. 2026, *A&A*, 707, A124, doi: [10.1051/0004-6361/202558423](https://doi.org/10.1051/0004-6361/202558423)
- Snowden, S. L., Mushotzky, R. F., Kuntz, K. D., & Davis, D. S. 2008, *A&A*, 478, 615, doi: [10.1051/0004-6361:20077930](https://doi.org/10.1051/0004-6361:20077930)
- Tamhane, P. D., McNamara, B. R., Russell, H. R., et al. 2023a, *MNRAS*, 519, 3338, doi: [10.1093/mnras/stac3803](https://doi.org/10.1093/mnras/stac3803)
- Tamhane, P. D., McNamara, B. R., Russell, H. R., et al. 2023b, *MNRAS*, 519, 3338, doi: [10.1093/mnras/stac3803](https://doi.org/10.1093/mnras/stac3803)
- Tamura, T., Kaastra, J. S., Peterson, J. R., et al. 2001, *A&A*, 365, L87, doi: [10.1051/0004-6361:20000038](https://doi.org/10.1051/0004-6361:20000038)

- Tanaka, K., Eckart, M., Fukushima, K., et al. 2026, PASJ, arXiv:2603.16263, doi: [10.1093/pasj/psag028](https://doi.org/10.1093/pasj/psag028)
- Tashiro, M., Kelley, R., Watanabe, S., et al. 2025, PASJ, 77, S1, doi: [10.1093/pasj/psaf023](https://doi.org/10.1093/pasj/psaf023)
- The Xrism Collaboration, Audard, M., Awaki, H., et al. 2026, Nature, 650, 309, doi: [10.1038/s41586-025-10017-x](https://doi.org/10.1038/s41586-025-10017-x)
- van Weeren, R. J., Osinga, E., Brunetti, G., et al. 2026, MNRAS, doi: [10.1093/mnras/stag054](https://doi.org/10.1093/mnras/stag054)
- Vazza, F., Angelinelli, M., Jones, T. W., et al. 2018, MNRAS, 481, L120, doi: [10.1093/mnrasl/sly172](https://doi.org/10.1093/mnrasl/sly172)
- Vazza, F., Brunetti, G., Kritsuk, A., et al. 2009, A&A, 504, 33, doi: [10.1051/0004-6361/200912535](https://doi.org/10.1051/0004-6361/200912535)
- Vikhlinin, A., Kravtsov, A., Forman, W., et al. 2006, The Astrophysical Journal, 640, 691, doi: [10.1086/500288](https://doi.org/10.1086/500288)
- Walker, S. A., Fabian, A. C., & Kosec, P. 2014, MNRAS, 445, 3444, doi: [10.1093/mnras/stu1996](https://doi.org/10.1093/mnras/stu1996)
- XRISM Collaboration, Audard, M., Awaki, H., et al. 2025a, ApJL, 982, L5, doi: [10.3847/2041-8213/ada7cd](https://doi.org/10.3847/2041-8213/ada7cd)
- XRISM Collaboration, Audard, M., Awaki, H., et al. 2025b, PASJ, 77, S242, doi: [10.1093/pasj/psaf055](https://doi.org/10.1093/pasj/psaf055)
- XRISM Collaboration, Audard, M., Awaki, H., et al. 2025c, Nature, 638, 365, doi: [10.1038/s41586-024-08561-z](https://doi.org/10.1038/s41586-024-08561-z)
- XRISM Collaboration, Audard, M., Awaki, H., et al. 2025d, ApJL, 985, L20, doi: [10.3847/2041-8213/add2f6](https://doi.org/10.3847/2041-8213/add2f6)
- XRISM Collaboration, Audard, M., Awaki, H., et al. 2025e, ApJL, 993, L11, doi: [10.3847/2041-8213/ae100c](https://doi.org/10.3847/2041-8213/ae100c)
- XRISM Collaboration, Audard, M., Awaki, H., et al. 2026, ApJ, 998, 210, doi: [10.3847/1538-4357/ae2c5c](https://doi.org/10.3847/1538-4357/ae2c5c)
- Zhuravleva, I., Chen, M. C., Churazov, E., et al. 2023, MNRAS, 520, 5157, doi: [10.1093/mnras/stad470](https://doi.org/10.1093/mnras/stad470)